Archaeological Prospection
Archaeol. Prospect. **21**, 277–291 (2014)
Published online 12 August 2014 in Wiley Online Library
(wileyonlinelibrary.com) DOI: 10.1002/arp.1489

Assessing the Condition of the Rock Mass over the Tunnel of Eupalinus in Samos (Greece) using both Conventional Geophysical Methods and Surface to Tunnel Electrical Resistivity Tomography

GREGORY N. TSOKAS[1]*, PANAGIOTIS I. TSOURLOS[1], JUNG-HO KIM[2], CONSTANTINOS B. PAPAZACHOS[1], GEORGE VARGEMEZIS[1] AND PETROS BOGIATZIS[1]

[1] *Laboratory of Exploration Geophysics, Department of Geophysics, School of Geology, Aristotle University of Thessaloniki, 54124, Thessaloniki Greece*
[2] *Mineral Resources Research Division, Korea Institute of Geoscience and Mineral Resources (KIGAM), 92 Gwahang-no, Yuseong-gu, Daejeon, 305-350, South Korea*

ABSTRACT The surviving Tunnel of Eupalinus comprises one of the greatest engineering achievements of ancient Greeks. The tunnel itself (1036 m long) was carved in the sixth century BC through solid rock by digging from both ends and advancing to the central meeting position. The method for achieving the meeting of the two simultaneously advancing branches is still unclear. The ancient lining shows damage, indicating instability of the rock mass, presumably due to tectonic action. At certain points, the damage becomes more severe and partial collapses are observed. Therefore, the monument is threatened and measures have to be undertaken to restore its stability and secure the safety of future visitors. The geophysical investigations reported here comprise part of a geotechnical study. The aim of the geophysical survey was to image the subsurface from the ground surface to the ceiling of the tunnel and, if possible, thereby provide information on the quality of the rock mass. A variety of well-established methods (VLF, self-potential, seismic refraction and electrical resistivity tomography) were used for this purpose, and also the relatively novel measuring approach of laying out electrodes in a 'tunnel to surface' mode. The latter method was an attempt for achieving tomographic imaging of the rock mass over the tunnel. Finally, the results of all the methods applied were combined and integrated in order to assess the tectonic regime above the Eupalinean Tunnel. Fractures and shear zones were detected and imaged. Further, the elastic moduli were determined at specific spots. In general, the geophysical interpretation matches well with the visible manifestations of the instabilities of the rock and provides clues for explaining their origin. The 'surface to tunnel' imaging provided increased resolution, which was a great advantage. Additionally, it is concluded that the construction of the tunnel was chiefly a product of survey method rather than consideration of geological factors. Copyright © 2014 John Wiley & Sons, Ltd.

Key words: Tunnel of Eupalinus; tunnel-to-surface ERT; ERT; elastic moduli assessment; multidisciplinary geophysics

Introduction

A most impressive ancient Greek technical construction that survives almost intact is the Tunnel of Eupalinus (also known as the Eupalinian Aqueduct; pronounced Efpalinos in Greek and alternatively spelt as Eupalinos and Efpalinos) in the island of Samos in Greece. The tunnel was used to channel the water into the walled urban complex of the ancient city of Samos, now called Pythagoreion.

The Eupalinian Aqueduct has been registered as a UNESCO world heritage monument, and a cleaning and restoration programme is currently aiming to make it accessible along its length. However, visible damage to the ancient lining, with collapses in some

* Correspondence to: G. N. Tsokas, Laboratory of Exploration Geophysics, Department of Geophysics, School of Geology, Aristotle University of Thessaloniki, 54124, Thessaloniki, Greece. E-mail: gtsokas@geo.auth.gr

Received 2 August 2013
Accepted 30 May 2014

places of the ancient construction being observed, reveals instability of the rock mass, suggesting that tectonic activity has affected the tunnel, therefore posing severe threats for its integrity and for the safety of visitors.

An assessment of the tectonic and geological regime in the area, in particular of the rock mass overlying the tunnel, should provide important information for the restoration. Therefore, a detailed geotechnical survey was carried out, including a geophysical investigation. The latter aimed to image the subsurface from ground level to the ceiling of the tunnel. Conventional methods (very low frequency (VLF), self-potential (SP), seismic refraction and electrical resistivity tomography (ERT)) were used, mainly along several profiles on the ground surface. Additionally, a relatively innovative approach was followed by obtaining electrical resistivity readings deploying electrodes both on the ground surface and inside the tunnel, in a form of 'tunnel to surface' tomography. This approach allowed the reconstruction of more accurate tomographic images compared with those produced only from ground-surface measurements. Finally, all the results were interpreted in a synergetic mode, leading to detailed mapping of the tectonic setting.

The Eupalinian Tunnel

The Eupalinian Tunnel is an impressive complex construction connecting two points 1036 m apart, dug into massive limestone (Figure 1). It is associated with about 895 m of duct connecting the water spring of 'Agiades' to the northern entrance, which is beyond the ancient city wall. Also, another 620 m of subterranean duct leave the southern entrance and drive the water to the fountains in the ancient city. The southern entrance lies in the walled part of the city. It was designed and constructed by the engineer Efpalinos, son of Nafstrofos from Megara during the sixth century BC (Herodotus: *Histories* 3.60).

The tunnel is the second oldest known that was excavated from both ends to meet in the centre: the oldest is Hezekiah's Tunnel in Jerusalem (ca. 700 BC), but this was excavated very close to the ground surface so that the two simultaneously advancing teams of tunnellers could hear loud banging to guide them (Frumkin and Shimron, 2006). Clearly, a geometry-based approach was used by Efpalinos to ensure that the advancing groups would meet successfully beneath ca.160 m of solid rock (Van der Waerden, 1968; Burns, 1971; Stiros, 2009).

This aqueduct system was used for about a 1000 years. It was rediscovered in 1853 by the French archaeologist Victor Guerin (1856) and surveyed by Fabricius (1884). It was cleaned and studied systematically by Kienast (1995, 2005). Today, about 100 m of the main tunnel starting from the south entrance are accessible to the public. The present study was performed in order to aid the restoration work, which will eventually make the tunnel accessible throughout its full length.

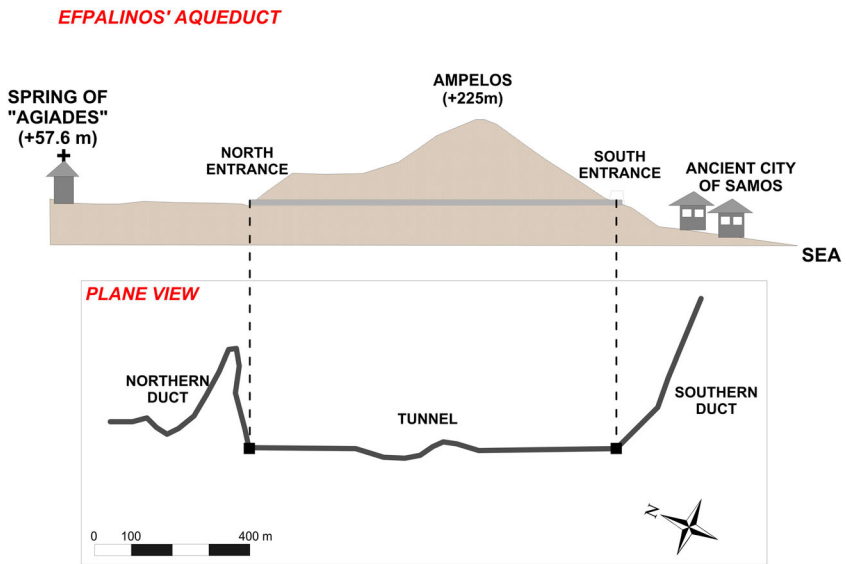

Figure 1. Schematic representation of the course of the ancient Eupalinian Aqueduct system. The main construction was a complex tunnel through the mountain, made by excavating the massive limestone simultaneously from both ends. Two buried ducts connect the ends to the springs and fountains, north and south of the tunnel, respectively. This figure is available in colour online at wileyonlinelibrary.com/journal/arp

DOI: 10.1002/arp

In the northern part of Figure 1, the medieval church of St John is founded on the ancient subterranean cistern that collected the water of Agiades springs. The water was channelled into an underground duct of 895 m length and a slope of 0.20% up to the northern end of the tunnel (Kienast, 1995; Psilovikos *et al*., 2003). In modern terminology, this part of the project was mainly achieved using the 'cut and cover' mode. This buried channel winds along the ravines until it meets the main tunnel.

The tunnel is dug entirely within a formation of lacustrine, medium to thick bedded, travertine-like limestones and thin-bedded marls, generally of monotonous sedimentation, with intercalations of red loam and clay and beds of tuffs and tuffites. In general, thick-bedded travertine-like limestones dominate the geology of the broader Pythagorion area (modern name of the ancient city of Samos). The tunnel floor is located at about 55.5 m above sea level (northern end 55.83 m; southern end 55.26 m; meeting point north 55.48 m; meeting point south 55.17 m; Kienast, 1995). The rock mass overlying the tunnel reaches a maximum thickness of 175 m, beneath 'Ampelos' hill (Figure 1).

On one side of the floor there is a trench (Figure 2), roughly 0.60 m wide and 3.8 m deep at the north end, which is extended to 8.9 m deep at the southern end. The slope of the trench is 0.36%, allowing the free flow of water in open-topped clay gutters. There are therefore essentially two tunnels. Nowadays, the upper and wider one can be walked through but only its southernmost 100 m are accessible to the public. The lower one containing the clay gutters has a constant width throughout. Portions of this water channel were roofed by stone slabs (Evans, 1999; Apostol, 2004) c. 3 m above the gutters. The space above them, up to the floor of the upper tunnel, was filled with rubble produced by the original workings. Therefore, plenty of space was available for inspection and repairs, and there are frequent shafts from the upper to the lower tunnel. The widespread occurrence of this type of underground construction in the Greek world suggests that the relevant techniques were well known (Doerpfeld, 1894; Burns, 1971).

The tunnel excavators were divided into two groups and advanced from both ends (Goodfield and Toulmin, 1965). They met at about the middle at a right angle. According to Kienast (1995), the mismatch of the two tunnels is about 0.4 m in the vertical and 0.7 m in the lateral direction, which in itself is a remarkable technical achievement: even by present standards (deviations of the order of 1 m are very common in modern underground constructions) the deviation is negligible.

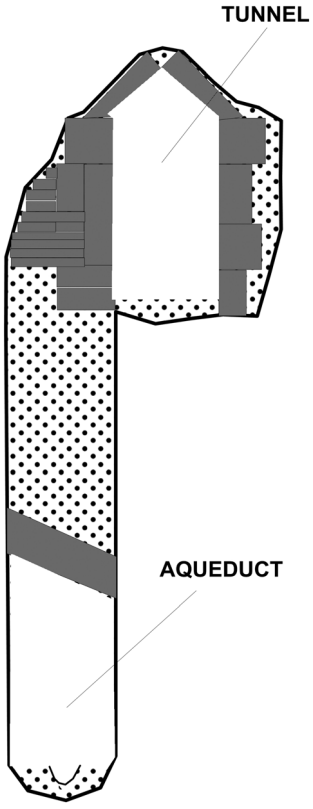

Figure 2. Cross-section of the main tunnel construction at a selected point, where the walls of the upper wider tunnel are dressed by stone lining. The tunnel is seen towards the south. The upper wider tunnel has a relatively irregular shape at this point, while the trench is about 4.5 m deep at its side. A terracotta pipe was put at the bottom of the trench to facilitate the water transfer towards the ancient city of Samos. (Modified from Kienast, 1995, 2005.)

Most of the length of the upper tunnel, which comprises the main and most impressive construction, is unlined. However, some parts were lined during the Archaic era when the tunnel was constructed and also during later Roman times, mainly because of the poor rock mass quality at some points. In particular, collapses have occurred where the tunnel crosses fault shear zones, mainly towards its edges. A photograph of the upper tunnel is shown in Figure 3; the metal grillwork covers the trench that leads to the lower tunnel.

A similar shallow buried channel was constructed to lead the water from the southern exit to the fountains of the ancient city. The length of this urban conduit is about 620 m and slopes at about 0.75%.

Survey lay out

Kienast (1995) established an arbitrary distance measuring system starting from a particular point at the northern entrance of the tunnel, placing nails at

DOI: 10.1002/arp

Figure 3. View of the main tunnel towards the north. The metal grillwork covers the trench of the lower tunnel. (Courtesy of K. Zambas.) This figure is available in colour online at wileyonlinelibrary.com/journal/arp

certain distances marked with tags. However, because many of these items were destroyed, new ones were installed for the purposes of the project presented here. Furthermore, we decided to use this system for reference not only for the survey in the tunnel but also for profiles established on the ground surface. As the work presented in these pages is georeferenced with respect to this system, we will refer to it as 'Local Distance Measuring System' and use the abbreviation 'LDMS' hereafter.

The traverses along which the various geophysical investigations were carried out are shown in Figure 4. With regard to the northern end (Figure 4 left), VLF was mainly used in order to locate fracture zones, which are present in the area and are presumably affecting the stability. The overlapped ERT and seismic lines aimed for a more reliable and meaningful engineering evaluation of the rock mass between the tunnel and ground surface. The SP line was conducted in the tunnel, but covering more or less the same length as the surface geophysics traverses, in order to detect possible water flows into the tunnel.

At the southern end, perpendicular lines rather than parallel to the tunnel were established. On one hand, this approach was imposed by the steep slope of the mountain cliffs, and on the other, a small length of the tunnel walls is dressed with lining at this end, suggesting that the rest has been opened through healthy rock. The only part of the tunnel accessible to the public comprises a length of about 100 m starting from the southern entrance. Thus, the rock mass over the small lined part close to the southern entrance needed further investigation. In fact the geotechnical inspection (Zambas, 2009) revealed the presence of a severe fracture at ca. 990 m.

The VLF survey

A number of VLF profiles were carried out on the slopes of the hill above the northern end of the tunnel (Figures 4 and 5). Their main target was to detect the exact location of major fractures and their associated shear zones within the limestone. Any additional quantitative information that could be deduced would be used in the following steps to further support the results of the tomographic techniques. The profiles

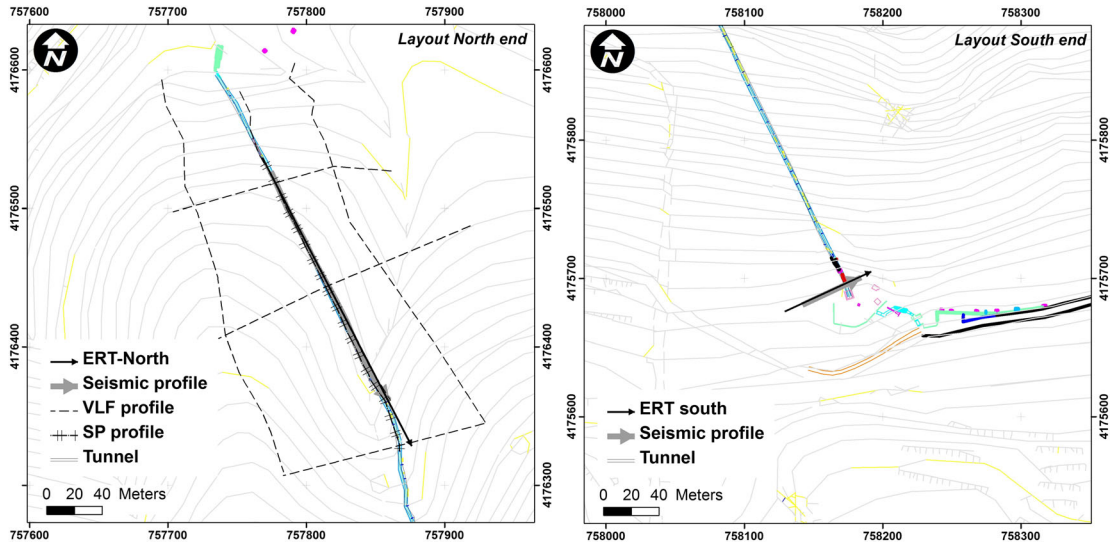

Figure 4. Global lay out of the lines along which geophysical measurements were taken for the various methods used. The purple dots northeast of the tunnel mark the location of the vertical shafts along the northern duct, which channelled the water from the spring of 'Agiades' to the northern end of the tunnel. This figure is available in colour online at wileyonlinelibrary.com/journal/arp

DOI: 10.1002/arp

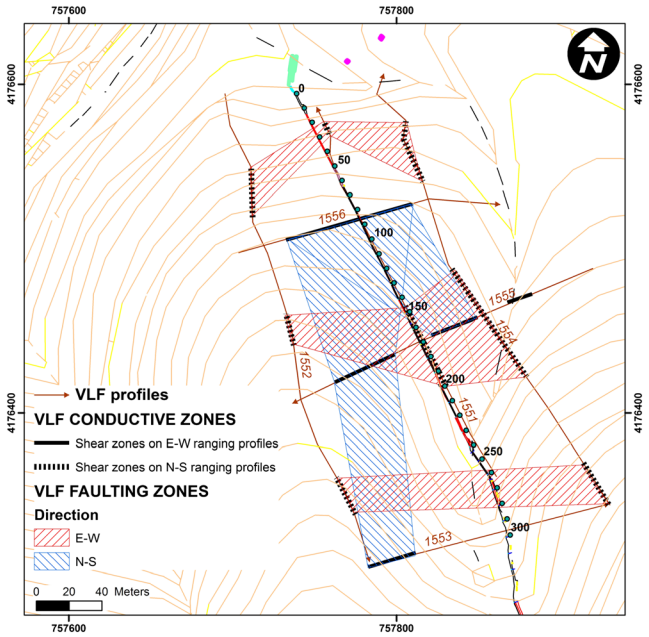

Figure 5. The VLF profiles established above the northern part of the tunnel are shown by continuous thin lines ending with arrows. The projection of the tunnel on the ground surface is also depicted, practically coinciding with VLF profile 1551. The detected shear zones are presented as dashed lines parts along the N–S profiles and thick continuous lines along the E–W progiless. The final interpretation is yielded by connecting shear zones having the same strike, depicted by areas filled with different coloured diagonal strips. Green points mark the 10-m stations of the Local Distance Measuring System (LDMS). Purple dots mark ventilation shafts of the northern duct. This figure is available in colour online at wileyonlinelibrary.com/journal/arp

were measured stepwise at 3 m intervals, using VLF broadcasts at 20.3 (ICV, Isola di Tavolara) and 21.75 KHz (HWU, Rosnay, French Navy). The ABEM Wadi system was utilized for the measurements. Readings were subjected to Fraser filtering (Fraser, 1969) and were then inverted to yield the parameters of the sources that cause the anomalies. Note that profile number 1551 practically coincides with the surface projection of the tunnel.

The interpretation of all VLF profiles is presented in an integrated manner in Figure 5. The detected shear zones (faulting zones) along each individual profile, in each direction separately, have been combined in Figure 5 and shown by areas of diagonal stripes. These are zones where the rock mass has been fragmented, due to tectonic movements causing the rock to fracture (faults). They have relatively low resistivities because they maintain more moisture than the healthy parts of the rock mass. By relating spatially the detected shear zones along the VLF profiles a map can be created (Figure 5) that can be considered a preliminary local tectonic map.

The fractures observed have both N–S (blue in Figure 5) and E–W directions (red). The E–W trending fractures intercept the tunnel at the positions 20–30 m and 260-280 m, whereas the N–S fractures cross the tunnel in a subparallel mode roughly at position 90–140 m. The region between the positions 150 and 200 m is of special interest because it seems to be tectonically very unstable, corresponding to the junction of two nearly perpendicular shear zones. It is expected that the rock material in this intersection has been extensively fractured, having thus a very high water permeability and reduced mechanical strength.

The tectonic regime initially assessed by the VLF survey controls the preferential water flow in the subsurface. In this respect, it is expected that problems would have been encountered during tunnel construction work. For this reason tomographic surveys were used, as the corresponding images were expected to provide additional details on this issue. At least the VLF method was able to identify the areas where the main fractures are located.

Ground-surface resistivity tomographies

Two electrical tomographic profiles annotated as ERT-North and ERT-south in Figure 6 were carried out above the northern and southern ends of the tunnel. The northern survey was deployed along the surface projection of the tunnel on the ground surface, while the southern one was located perpendicular to the tunnel orientation. The latter choice was imposed by the local topography, which did not allow the establishment of a tunnel-parallel line. Moreover, the northern ERT tomography covers the main part of the tunnel that is lined. As previously explained, lining was needed for the parts of the construction where the rock mass was relatively weak and fractured.

As the depth of the target was known, the ERT were set up in such a way as to penetrate at least to the upper tunnel floor. Therefore, there was a compromise between the appropriate length of the electrode array and the maximum resolution, taking into account that the equipment used supported 48 electrodes. Considering these factors, we utilized an interprobe distance of 5 m, which resulted in a penetration depth of roughly 50 m. With respect to the LDMS, the tomography starts at the surface projection of position 65 m and ends at the projection of position 300 m. Due to the different resolving capacity of the respective ERT configurations, data were collected using the dipole–dipole, the pole–dipole (forward and reverse) and the Wenner–Schlumberger electrode arrays. The three data sets were processed individually but then were also processed as a unified dataset in order to produce

DOI: 10.1002/arp

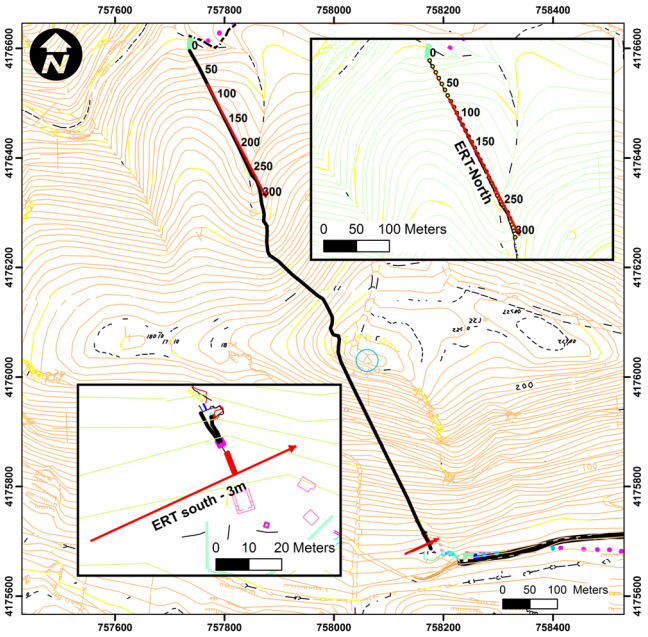

Figure 6. Position of the two ERT profiles carried out on the ground surface above the Eupalinus Tunnel. The tunnel is represented by the black line and some distances of the LDMS are also marked in the figure. The inset maps show the ERT transects in greater detail. This figure is available in colour online at wileyonlinelibrary.com/journal/arp

enhanced resolution results (Athanasiou *et al.*, 2007a). As previously explained, because of the limited available space, the tomography at the southern entrance was measured using only 24 channels spaced 3 m apart from each other; several arrays were used to collect the data, which were then jointly inverted following the same approach as for the data from the northern end. Geoelectrical measurements were collected using the 10-channel SYSCAL-pro resistivity meter (IRIS Instruments) using custom multicore cables.

A standard smoothness-constrained inversion approach was followed for the inversion of the ERT data (Tsourlos, 1995), using the DC2DPRO geoelectrical inversion package (Kim, 2009). The software is based on a finite-element forward solver and applies a smoothness-constrained inversion scheme using the active constrained balancing technique (Yi *et al.*, 2003). The relatively small root mean square (RMS) errors (3–4%) produced by all inversions suggests a generally good quality of the measurements collected.

The distribution of the resistivity along the ERT-North profile is presented in Figure 7 along with the filtered real and imaginary components of the VLF response for profile 1551, as the tomographic transect and the VLF profiles are subparallel with a small shift. A series of fractured zones can be inferred from both methods, which are depicted by black dashed lines in Figure 7. On the ground surface these zones are found at positions of about 90, 185, 220 and 257 m, while at depth they appear to intersect the tunnel it positions 95, 165, 185 and 235 m, respectively. Clearly, both methods have produced compatible and complementary results, a fact that strengthens the proposed interpretation. The tomographic imaging of the rock mass overlying the tunnel reveals the existence of extended low-resistivity areas, which probably formed by the action of the fractures. These are presumably shear zones that extend down to the level of the tunnel and therefore will affect it. Obviously, these zones are, in general, the main reason for the failures observed on the lining and in the tunnel construction.

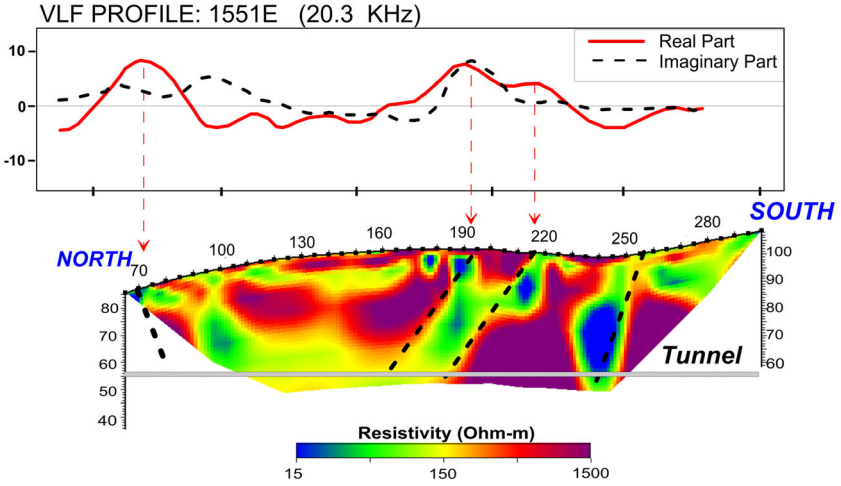

Figure 7. Unified array (data from dipole–dipole, pole–dipole (forward and reverse) and Wenner–Schlumberger) resistivity tomography ERT-North (lower figure) and its comparison to the filtered real (continuous line) and imaginary (dotted line) VLF components (upper figure). The dashed black lines represent the inferred fault zones. The tunnel has been also drawn on the tomographic image. This figure is available in colour online at wileyonlinelibrary.com/journal/arp

DOI: 10.1002/arp

The same processing and interpretation approach was utilized for the ERT line at the south end of the tunnel (see Figure 6), which aimed to investigate the general geotechnical conditions in this area. The results of the inversion of the dipole–dipole, pole–dipole and combined array data sets (dipole–dipole and pole–dipole) are shown in Figure 8, with the tunnel being depicted in each section by a rectangle at the appropriate location. It is clear that the inversion results of the individual arrays are somehow different, but this is to be expected if we consider the different sensitivity and resolving ability that the various arrays exhibit (Athanasiou *et al.*, 2007a).

Overall the result of the combined array depicts significant resistivity variations. Two main low-resistivity areas, probably corresponding to almost vertical fractured zones, are observed between positions 21–30 m and 45–57 m. It appears that the south tunnel entrance has been excavated within the easternmost fractured zone and this justifies the thick lining encountered at that part of the tunnel.

An interesting feature is that the high resistivity anomaly corresponding to the tunnel itself is almost unrecognizable in the dipole-dipole and pole-dipole inverted sections of Figure 8a and b. This is to be expected given the size of the tunnel cross-section (ca. 2 m), which is comparable to the 3-m interelectrode spacing used. However, in the case of the jointly inverted image of the combined array dataset (Figure 8c), the high resistivity anomaly of the tunnel is just visible, verifying that the combination of different electrode arrays can improve the resolving ability and reliability of the ERT technique.

Surface-to-tunnel electrical resistivity tomography

It is well established that surface ERT measurements suffer from reduced sensitivity as depth increases. In

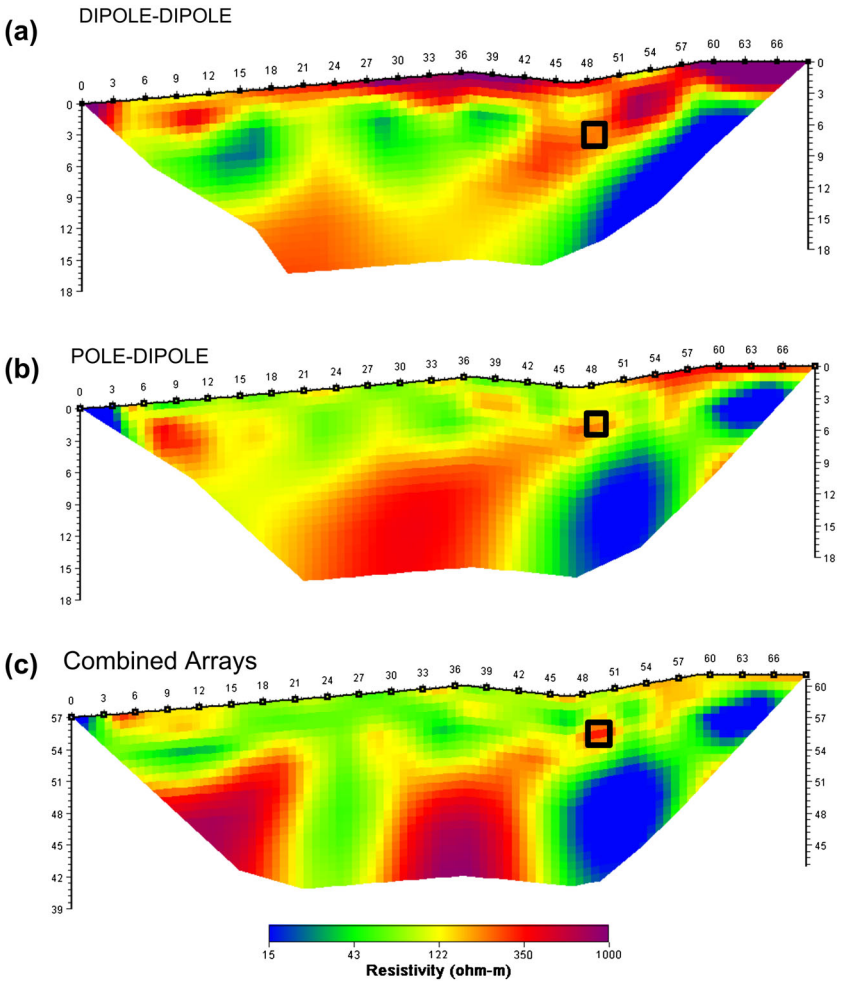

Figure 8. Inversion of the data of different electrode arrays along the ERT-south profile. (a) dipole–dipole, (b) pole–dipole, (c) combined dipole–dipole and pole–dipole. The tunnel is represented by a small square outlined. This figure is available in colour online at wileyonlinelibrary.com/journal/arp

DOI: 10.1002/arp

the case of the ground-surface ERTs at the Eupalinian Tunnel, which is situated on average 50 m below the ground surface, it follows that the reliability of the inverted ERT images at the area near the tunnel is somehow limited. To improve resolution with depth we also deployed electrodes within the tunnel and applied ERT measurements in a surface-to-tunnel mode. Note that only a very limited application of such a measuring mode has been reported in the literature, describing either surface-to-tunnel (Sasaki and Matsuo, 1993) or tunnel-to-tunnel (Van Schoor and Binley, 2010) application of geoelectrical measurements for deep-mining prospection purposes.

A sketch of the electrode arrangement used in the Eupalinian Tunnel measurements is provided in Figure 9. The electrodes are positioned both in the tunnel and on the surface at a spacing interval of 5 m. The section starts at position 65 m and extends up to 180 m, comprising 24 electrodes in the tunnel and 24 electrodes on the surface. Note that the positions of the electrodes on the surface are identical to the positions used for the ground surface ERT and that the tunnel electrode locations are the orthogonal projections of the respective surface electrodes.

The only additional piece of instrumentation that was used in the case of 'surface to tunnel' measurements was a 200-m-long, 24-channel, extension cable. This was necessary for the connection of the instrument with the in-tunnel electrode array.

The tunnel electrodes were positioned at an elevation of 1.10 m above the tunnel floor at the part of the tunnel that is covered with archaic lining, as can be seen in Figure 10. Bentonite mud with some salt added was used as an electrode, as this kind of electrical coupling has been proven to have an excellent function (Athanasiou *et al*., 2007b; Tsokas *et al*., 2006; Tsokas and Tsourlos, 2007; Tsourlos and Tsokas, 2007, 2011).

Figure 10. The measuring tape attached to the western wall of the Eupalinian Tunnel, 1.1 m above the floor, marks the tomographic transect that was carried out. The bunch of connecting cables is also shown. Electrodes were composed of bentonite mud mixed with salt (Tsokas *et al*., 2006; Athanasiou *et al*. 2007b; Tsokas and Tsourlos, 2007; Tsourlos and Tsokas, 2011). This figure is available in colour online at wileyonlinelibrary.com/journal/arp

One of the issues that required investigation is how much the tunnel (void) affects the in-tunnel measurements. This is essential because if the effect in the tunnel was high, some action would be needed in order to either correct the data or include the tunnel within the interpretation procedure. To provide an indication of the tunnel effect, calculations were performed for the potential variation for various electrode separations under the realistic assumption that the initial electrode spacing is five times larger than the tunnel radius (spacing = 5 m and tunnel radius = 1 m). The calculations of the percentage error introduced by the tunnel for homogeneous ground and for increasing electrode separations were performed using the software of an analytical solution (Wait, 1982) and are shown in Figure 11. Results suggest that generally

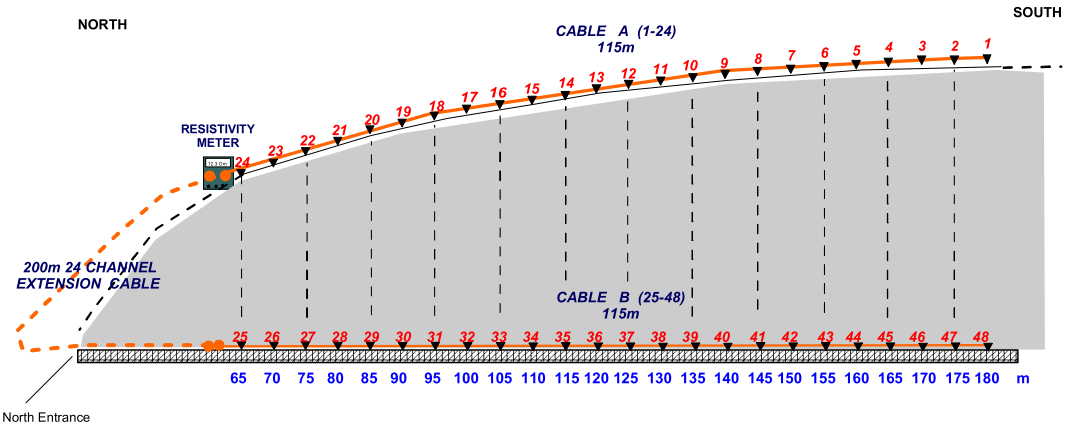

Figure 9. Sketch of the electrode arrangement used for the surface-to-tunnel ERT measurement. This figure is available in colour online at wileyonlinelibrary.com/journal/arp

DOI: 10.1002/arp

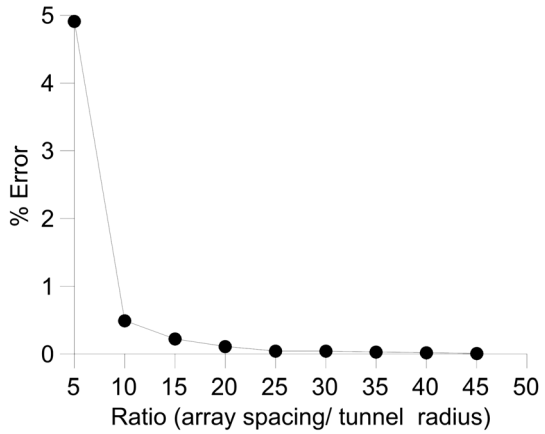

Figure 11. Error introduced by the tunnel effect for different electrode separations.

the tunnel effect is limited and can be ignored without introducing severe errors within the measurements.

Measurements were performed using the pole–dipole array as shown in Figure 12. The entire data-set involved measurements including electrodes only on the ground surface (Figure 12a), only in the tunnel (Figure 12b) and electrodes both on the surface and in the tunnel (Figure 12c and d). This last category can be separated into measurements consisting of current injection in the tunnel and potential readings on the ground surface (Figure 12c), and vice-versa (Figure 12d). Therefore, it can be considered that the entire dataset consists of four distinct sets.

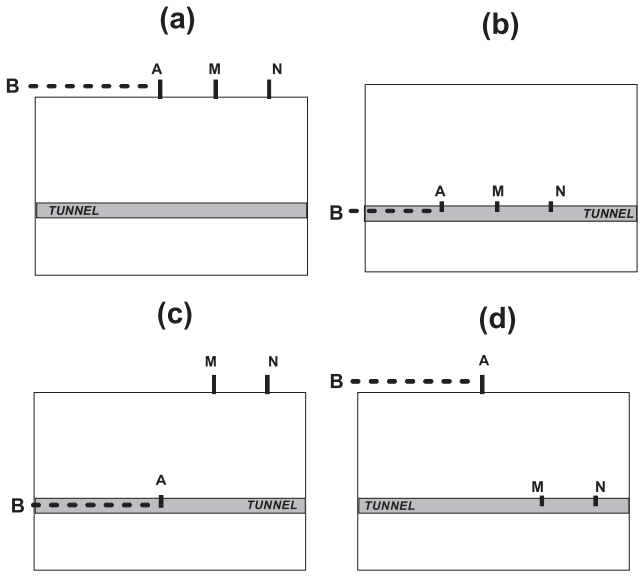

Figure 12. Different pole–dipole electrode layouts corresponding to the different measuring modes. The dataset that was inverted to yield the resistivity distribution in the area between the tunnel and the ground surface consisted of the measurements of all array types.

The dataset collected was inverted using the standard inversion software. As the tunnel itself is not included into the inverted model, the tunnel electrodes are incorporated as borehole electrodes. The inverted geoelectrical image is shown in Figure 13.

The result of this tomography provides a more complete picture for the space between 60 and 80 m compared with the respective surface array. The fractured zone at the location of 95 m that is only partly seen in the inverted ground surface tomography results (Figure 7) (detected by the VLF also), is now depicted clearly in the tunnel-to-surface mode. Evidently it transects the tunnel at about 95–100 m.

At about 70 m another low resistivity zone is observed, which extends to 80 m. This zone is hardly recognizable on the ground surface ERT (Figure 7), but it produces a pronounced VLF signal. It seems to extend down to the level of the tunnel and even below that. Thus, the tunnel-to-surface tomography complemented the results of the northernmost part of the ground surface ERT.

In addition, in the tunnel-to-surface inverted image (Figure 13) a conductive zone almost parallel to the tunnel between 70 and 55 m a.s.l. can be clearly seen extending from the 95 m to 175 m of the section, which is in good agreement with the surface array information of Figure 7.

The resistivity below the tunnel appears to be moderate for the surface ERT (Figure 7), while for the surface-to-tunnel arrangement the same area exhibits high values (Figure 13). This is an outcome of the highly reduced sensitivity of the surface array for the

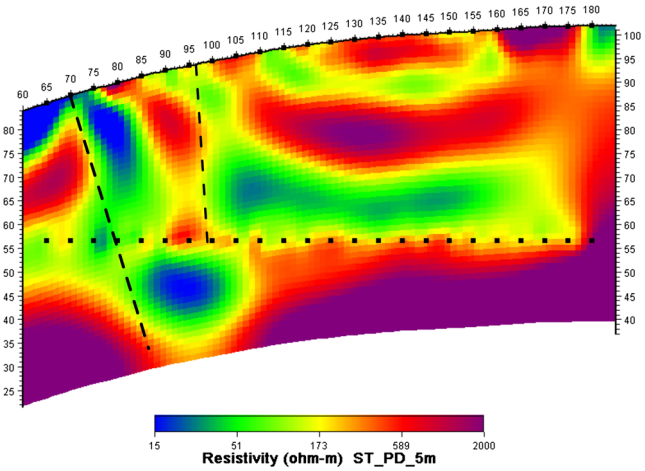

Figure 13. Resistivity distribution in the rock mass lying between the Tunnel of Eupalinus and the ground surface yielded by inversion of the surface-to-tunnel dataset. In fact, four distinct data sets were combined to produce this image, each of them using one of the different electrode configurations shown in Figure 12. This figure is available in colour online at wileyonlinelibrary.com/journal/arp

DOI: 10.1002/arp

area under the tunnel, in contrast to the surface-to-tunnel ERT, which has excellent sensitivity for the same area because of the electrodes deployed in the tunnel.

Overall, the surface-to-tunnel array results produced inverted images of increased resolution, demonstrating that this technique can offer a better insight of prospected targets.

The seismic survey

A seismic line with an approximate length of 240 m was shot over the projection of the northernmost part of the tunnel, as shown in Figure 14. This line extends from position 50 m to ~290 m, coinciding with the larger section of the ERT-North tomography. The line was surveyed using arrays of 48 geophones in a roll-along mode, utilizing a geophone distance of 2.5 m. The particular seismic line layout was selected in order to cover the lined part of the tunnel, that is, the same reason for which the coincident ERT was designed. Both *P* and *S* waves were produced by using a sledge hammer. The trivial method of striking against the face of a beam laid perpendicular to the line of geophones

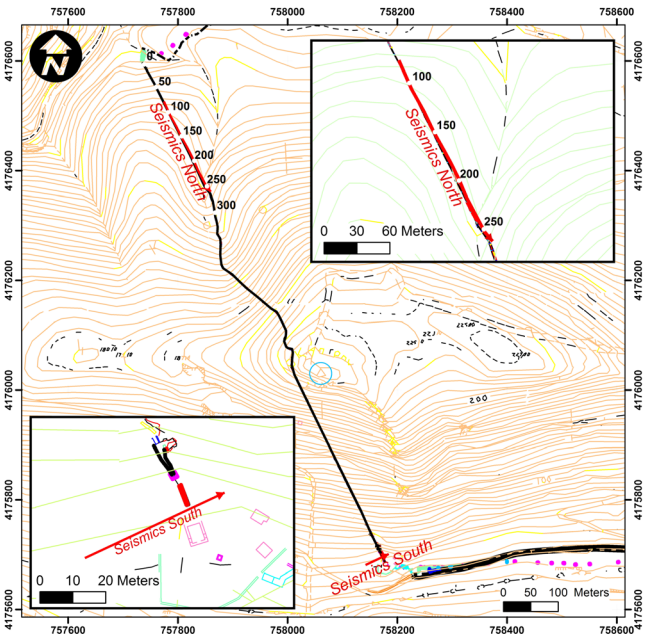

Figure 14. Overview and detailed layout (insets) of the seismic lines shot above the northern and southernmost sections of the tunnel. The northern seismic line covers the projection on the ground surface of the lined part of the tunnel having approximately the same direction and length as the ground surface ERT. The south seismic line was located just behind the small stone house serving as tourist entrance to the tunnel. In the inserted lower left figure, the thick red line depicts the staircase that leads to the tunnel, whose plan-view is shown with thick black lines. Notice that the tunnel's southern end is relatively wider than its typical dimensions (1.8x1.8 m). This figure is available in colour online at wileyonlinelibrary.com/journal/arp

was used for the generation of *S* waves. Various shot-points were located in the centre of the line, as well as between geophones at a number of positions. Additional shots were placed at the ends of the line, as well as at various offsets from the line. In this way, a large number of records were produced, corresponding to a dense coverage that allowed study of the velocity structure in detail.

The roughness of the terrain prevented the establishment of a line parallel to the tunnel at the southern end. Thus, a seismic line was shot almost perpendicular to the course of the tunnel (Figure 14), in an identical way as that at the northern end, but the spread involved 24 geophones (2-m intervals).

A StrataView (Geometrics Inc.) seismograph was used (48 channels), along with standard refraction geophones and cables. The first breaks were picked up for each shot and the travel-time versus distance curves were constructed. When interpreting the travel-time curves, arrivals were attributed to possible refractors, thus providing the data for application of the general reciprocal method (GRM; Parker, 1986). In this way, an initial layered model was derived that was considered as input for subsequent tomographic data treatment, following the approach of Soupios *et al*. (2001).

Regarding the northern line, Figure 15 shows the model inferred for the distribution of seismic velocities in the rock mass for both types of body waves. In general, almost no discrepancies are observed between the results of *P* and *S* waves, despite the fact that the corresponding models originate from independent readings and interpretations. Lateral model discontinuities are observed at ca. 80 and 110 m, interpreted as fractures/faults. The first one corresponds to the low resistivity zone detected by the VLF profile and the tunnel-to-surface ERT from about 70 to 80 m. It appears to affect the rock mass deeper than the second one and, although not seen here, we can say that it extends down to the tunnel level judging by the resistivity image (Figure 13).

The zone of low values seen on the ground resistivity tomography (Figure 7) at ca. 185 m (extending to ca. 220 m) is also identified here as a relatively broad, shallow, zone of low velocities. This area has a rather orthogonal shape, similar to the area of very low resistivities found in the ERT tomography between 170 and 220 m and an elevation of ~80 m (see Figure 7). This correlation is expected, because fragmentation of the rock material reduces its mechanical strength and facilitates the concentration of water and thus the resistivity is reduced. Moreover, a sharp discontinuity is observed, especially in the P-wave model, at position 255–260 m, in excellent correlation with the similar

DOI: 10.1002/arp

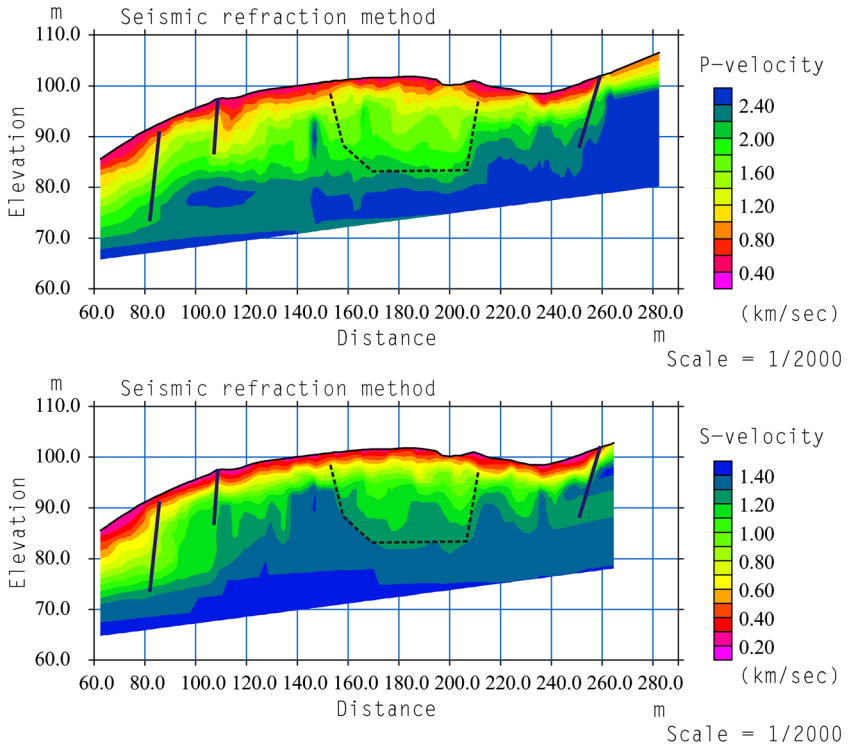

Figure 15. *P*-wave (top) and *S*-wave (bottom) velocity models obtained from the surface seismic profile above the northern end of the Eupalinian Tunnel. Solid lines depict major lateral discontinuities (possible faults), whereas the dashed line identifies a wide area of lower elastic moduli of the limestone above the tunnel, in good correlation with corresponding ERT results. This figure is available in colour online at wileyonlinelibrary.com/journal/arp

north-dipping discontinuity of the ground surface ERT profile (Figure 7).

In general, the rock mass above the tunnel exhibits an expected significant variation of elastic properties, with the shallower part of the formation exhibiting very low velocities (V_P = 0.4–0.8 km s^{-1} and V_S = 0.2–0.5 km s^{-1}), corresponding to very low elastic moduli. Underlying this overburden, a weathered rock layer is observed (V_P = 1.0–1.8 km s^{-1} and V_S = 0.6–1.0 km s^{-1}). The relatively healthier rock mass can be found at greater depths (typically at a depth of 10–20m from the ground surface), although we are lacking resolution at depth, where refracted rays travel almost horizontally. On the other hand, the lateral distribution of velocities is relatively inhomogeneous due to the role of fractures, as previously described.

Of course the subsurface at the northern part of the Tunnel of Eupalinus is not differentiated lithologically but it appears to have varying mechanical properties, both with depth and laterally because of weathering and tectonic action. Thus, we can conventionally distinguish various 'geotechnical units' and describe them as 'layers' for assessment of their mechanical properties. The estimates of the varying mechanical properties are shown in Table 1, which are of course based on the relevant variations of the velocity of the *P* and *S* waves.

Table 1. Indicative values of seismic velocities and elastic moduli. The classification into 'layers' (geomechanical units) is arbitrary based on the division of the range of *P*-wave velocity into increments of either 250 or 300 m s^{-1}.

Layer	V_S (m s^{-1})	V_P (m s^{-1})	*G* (Mpa)	*E* (MPa)
1	450	900	400	1100
2	750	1300	1300	3300
3	1000	1700	2400	6000
4	1250	2100	4000	9500

G, shear modulus; E, Young's modulus.

Figure 16a and b depicts the corresponding *P* and *S* velocity models over the southern entrance of the tunnel. Due to the limited spatial extent of the profile, the corresponding velocities have been grouped into three classes, representing three main units. The first unit corresponds to the surface cover, which exhibits a thickness of a few metres and low velocities (V_P = 0.4 km s^{-1} and V_S = 0.2 km s^{-1}), similar to the north profile. This formation is underlain by limestone in the western part (left-hand side) of the cross-section, showing much higher velocities (V_P = 2.0 km s^{-1} and V_S = 1.35 km s^{-1}), with values very similar to the deeper part of the northern profile, indicative of relatively healthy bedrock. This formation abruptly changes at ca. 40–45 m and a unit with much lower

DOI: 10.1002/arp

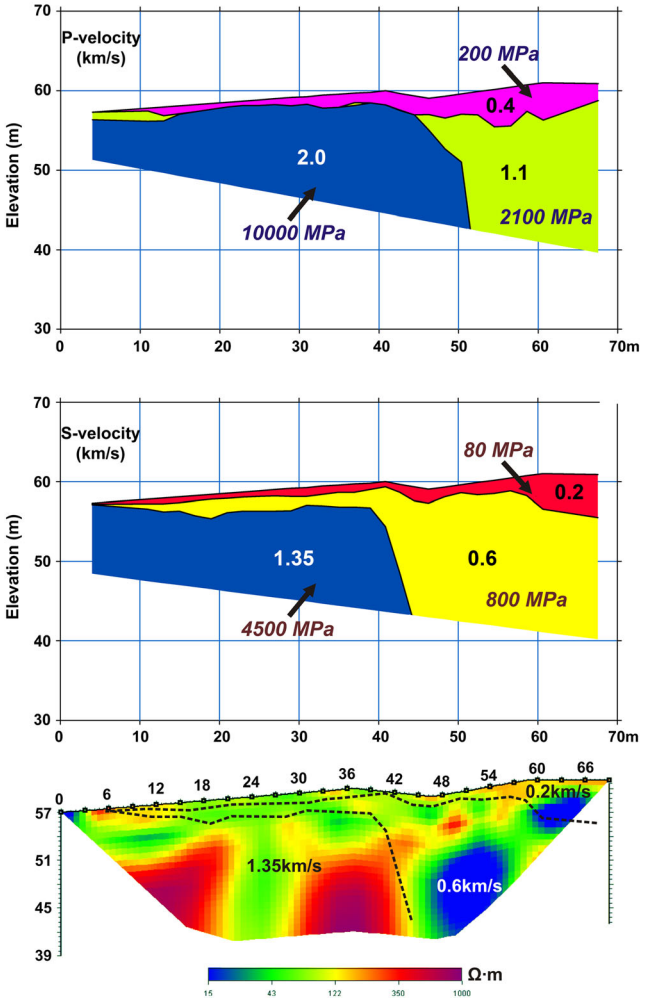

Figure 16. Models obtained from *P*-wave (top) and S-wave (middle) arrivals for the structure of the subsurface along the line perpendicular to the southern end of the Eupalinian Tunnel. The model results are the outcome of the inversion process (Soupios *et al*., 2001) using the General Reciprocal Method's results as input. The velocities are in km s^{-1}. The lower drawing shows the respective ERT (Figure 8) where the boundaries of the geological units inferred by *P*-waves (upper drawings here) have been superimposed. Estimates of Young's modulus E are shown along the model derived from compressional (P) waves (top) whereas estimates of the shear modulus G are shown with the model from the shear waves. This figure is available in colour online at wileyonlinelibrary.com/journal/arp

velocities ($V_P = 1.1$ km s^{-1} and $V_S = 0.6$ km s^{-1}) dominates the eastern part of the section. This low-velocity formation coincides with the low-resistivity formation of the corresponding ERT. This is clearly depicted in Figure 16c, where the boundaries of the units observed in the V_S profile (controlling the shear modulus) are superimposed on the corresponding ERT tomography. From this combined interpretation we can infer that this rock mass quality change is most probably controlled by the presence of a fault, which also has a surface manifestation. The tunnel has been excavated in this less stable, highly fractured bedrock, which has greater hydraulic permeability than the healthy limestone in the west. Note that the southern end of the tunnel is dressed with lining for a short distance only, which coincides with the observed weakness of the rock mass. Seismic velocities and indicative elastic moduli of the units at the southern end of the tunnel are listed in Table 2.

The SP survey

Using geophysical prospecting methods to image the area behind walls, and if possible study their condition in terms of moisture content, has been proven to be an inexpensive, fast and relatively easy procedure (Colla and Maierhofer, 2000; Cosentino and Martorana, 2001; Karastathis *et al*., 2002; Sass, 2005; Sass and Viles, 2006; Viles *et al*., 2008; Mol and Preston, 2010; Tsourlos and Tsokas, 2011).

In our case, it was decided to also carry out an SP (self potential or spontaneous polarization) survey inside the tunnel by placing the potential probes on the walls. Three traverses were measured starting at 62.5 and ending at 300 m (LDMS, Figure 17): one on each wall at a height of 1.10 m and one on the floor. Measurements along the traverses were performed in a continuous mode irrespective of the existence or not of lining. The aim was to detect anomalies that could be linked to water flow.

The data were smoothed and regional trends were removed. Then they were averaged out for each particular position and the result is shown in the inset plot of Figure 17. The variation of SP between 62.5 and 300 m is shown in Figure 17 by the scatter of dots representing the readings. A pronounced anomaly is observed at ca. 240–250 m suggesting that water flows from the fracture zone into the tunnel at this position because it has a positive character. This is in agreement with the subsurface images yielded by the other geophysical methods (Figures 7 and 13).

A small ravine with a stream trace lies above the tunnel at about 240–250 m, as seen in the topographic map comprising the background of Figure 17. We

Table 2. Indicative values of seismic velocities and elastic moduli for the three main formations at the southern end of the Eupalinian Tunnel. The arbitrary classification into geomechanical units (layers) is based on the division of the range of the *P*-wave velocity into increments of 400 m s^{-1}.

Layer	V_S (m s^{-1})	V_P (m s^{-1})	*G* (Mpa)	*E* (MPa)
Topsoil	200	400	80	200
Fractured bedrock	600	1100	800	2100
Healthy bedrock	1350	2000	4500	10000

G, shear modulus; E, Young's modulus.

DOI: 10.1002/arp

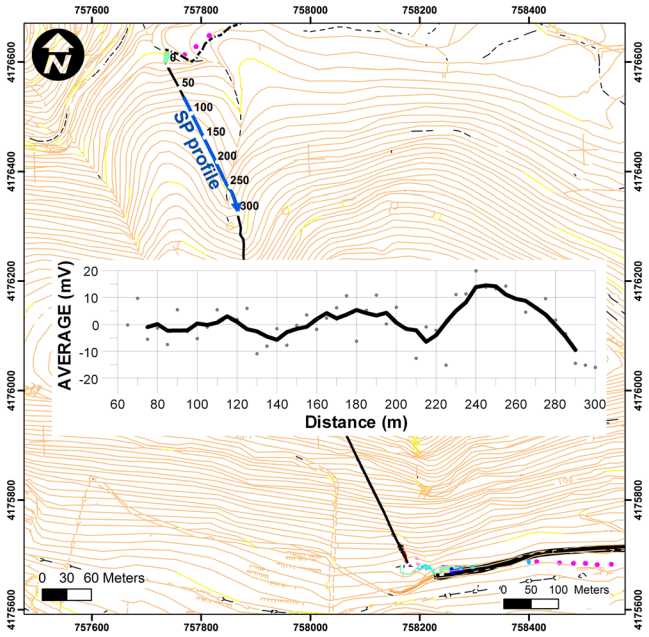

Figure 17. The SP traverses were performed from point 62.5 to point 300 m: this part of the tunnel is indicated by the blue arrow. The average SP variation of all three traverses is given in the inserted plot. The relatively large and strong positive peak at about 240–250 m is attributed to water outflow into the tunnel, an interpretation that is compatible with the other geophysical results. This figure is available in colour online at wileyonlinelibrary.com/journal/arp

consider that this is a surface manifestation of the shear zone that creates the resistivity and velocity discontinuity in Figure 18. Thus, all the data are in agreement and indicate that water is supplied from the ravine to the shear zone and flows into the tunnel.

Discussion

The multidisciplinary geophysical investigations aimed to assess the quality of the rock mass between the ground surface and the level of the tunnel. Despite some minor discrepancies, the subsurface models obtained from all surface geophysical methods (VLF, surface ERT, tunnel-to-surface ERT, seismic refraction and SP) are in reasonable agreement.

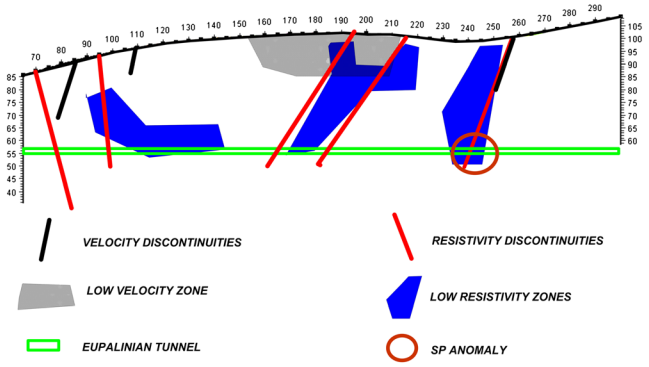

Figure 18. Sketch of the subsurface at the northern end of the Eupalinian Tunnel from the combined interpretation of all methods used. This figure is available in colour online at wileyonlinelibrary.com/journal/arp

The basic assumption for proceeding to an integrated interpretation scheme was that shear zones are expected to produce a low-resistivity signature, as well as low *S*-wave velocity areas (smaller shear elastic moduli). This pattern is reasonable to expect because a shear zone would exhibit high hydraulic permeability (hence possible relatively high water content) and reduced mechanical strength. Therefore, areas with low-resistivity anomalies and where low seismic velocities were detected, were mapped (Figure 18). In addition, the major discontinuities detected by the various geophysical models and the water-flow region detected by the SP survey were also mapped in the same figure.

Figure 18 exhibits several interesting features. The first concerns the fact that seismic estimates are confined to the upper 25–30m, due to the limited depth penetration of that technique (see also Figure 15). On the other hand, ERT estimates exhibit a greater depth extent (see Figures 7 and 13), reaching the tunnel itself. The agreement between the different methods varies along the rock mass above the tunnel. The most robust feature is the major discontinuity at 255–260 m on the surface, crossing the tunnel at 240–245 m. This discontinuity is identified by all geophysical models, including the SP measurements, and seems to involve major water flow. This observation is in excellent agreement with the distorted roof slab observed inside the tunnel at ~245 m (Zambas, 2009).

Moving to the central part of the interpretation drawing, the resistivity tomography identifies a major low-resistivity zone at ~195–215 m on the surface, which transects the tunnel at ~165–190 m. This anomaly only partly coincides with the low-V_S region on the surface identified in the seismic model: although the two anomalies share the same southern edge (~215 m), the seismic anomaly also extends to ~155 m towards the north. The identified cross-section of this 'weak' zone almost coincides with the cracking of the roof lining seen at ca. 178–200 m (Zambas, 2009).

The largest discrepancies are observed towards the northern edge of the tunnel, where the discontinuities identified by seismic and resistivity methods show a very poor correlation. The deeper resistivity anomaly cannot be correlated with seismic information due to the shallower penetration depth of the seismic survey. Such discrepancies can be due to several causes, such as geophysical modelling errors (e.g. two-dimensional topography-edge effects close to the more steep

DOI: 10.1002/arp

northern part of the tunnel). Other causes could be responsible, for example, mapping of geological/geotechnical formation with different properties that do not follow the low-resistivity/low-V_S pattern proposed: a typical example being the presence of a fractured zone with low water content, showing low-V_S values but high resistivities.

On the other hand, despite the observed differences, the results suggest the presence of several discontinuities reaching the tunnel at ~75–100 m, as well as low resistivities directly above the tunnel between ~95–140 m. This extended fractured/low-resistivity area is in very good agreement with the ancient repairs at 110 m and the roof fall observed at 130 m (Zambas, 2009). The presence of an extended zone of low-quality rock explains why the walls of the tunnel were dressed with lining in the northern part, as the ancient workers were presumably facing the problem of digging through low quality rock mass. Extended subsidence is also seen between 48 and 62 m, while water flows into the tunnel at 65–75 m, 100–110 m and 135–178 m (Zambas, 2009). Note that the geophysical data practically do not provide information before 70–75 m due to edge effects; hence no correlation can be considered for this tunnel section.

The observations performed for the northern part of the tunnel can be similarly extended to the southern part, where tunnellers would had excavated the low-quality rock almost from the start of their effort, as evident from the lining present. Indeed, fractures are observed almost everywhere in the southernmost part (Zambas, 2009). This observation is confirmed by Figures 8 and 16, which show that the tunnel lies within very low-V_S (~600 m s^{-1}) and low-resistivity (15–45 Ohm.m) material, indicative of poor quality rock material in this tunnel section. Clearly, these observations coincide spatially with the zones of low rock quality as obtained by the geophysical investigations. This fact strengthens our assertion that the geophysical images are realistic. Further, it is seen that the geophysical methods have a complementary role with the engineering observations because they provide imaging of the 'unseen' areas of the rock.

It is emphasized that our aim was the assessment of the quality of the rock mass and not to extract historical and archaeological conclusions. However, the geophysical surveys have added some clues to the method of design and construction. The tunnel seems to cross successively weak and healthy zones of the limestone rock mass at the northern end and does not follow any geological or tectonic contact. Thus, the solution to the problem of alignment of the two simultaneously advancing tunnels must have been found by geometry and surveying (Apostol, 2004; Stiros, 2006, 2009, 2011).

Conclusions

Well-established geophysical methods along with a relatively innovative one were used to assess the tectonic and geotechnical features above the northern and southern end of the Eupalinean Tunnel in Samos. Fractures and areas exhibiting weak mechanical strength (shear zones) were detected and imaged.

This study shows the potential of geophysics in assisting and guiding geotechnical interventions aiming to recover the lost stability of monuments due to tectonic action. The geotechnical survey was greatly aided in proposing the correct measures for restoring and securing the construction.

The integrated use of geophysical methods and the synergetic interpretation proved once more to be a valuable tool to define the exact danger that threatens a unique monument. The increased resolution of the 'surface to tunnel' imaging is an additional advantage with these methods. Finally, the research indicates that the construction of the tunnel was chiefly a product of survey method rather than consideration of geological factors.

Acknowledgements

We are grateful to Egnatia S.A. for financing the project and in particular to George Aggistalis, engineering geologists of the company, who inspired us and he was also the moving force of all the studies regarding the restoration of the Eupalinian tunnel. His continuous concern and fruitful comments helped us to design the survey and interpret the results.

We also thank the architect Constantinos Zambas and Mrs Maria Viglaki, director of the 21st Ephorate for Prehistoric and Classical Antiquities.

We are greatly indebted to Dr. Chris Gaffney for editing the manuscript and taking care for the correct English spelling and grammar. His critical view contributed essentially to the final appearance of this paper.

The third author was supported for his sabbatical in Greece by the Basic Research Project of Korea Institute of Geoscience and Mineral Resources is in turn funded by the Ministry of Science, ICT & Future Planning, Republic of Korea. Therefore, all authors had the opportunity to work together in designing and implementing the project presented in these pages. For this reason, we feel grateful to the above mentioned organization.

DOI: 10.1002/arp

References

Athanasiou EN, Tsourlos PI, Papazachos CB, Tsokas GN. 2007a. Combined weighted inversion of electrical resistivity data arising from different array types. *Journal of Applied Geophysics* **62**(2): 124–140.

Athanasiou EN, Tsourlos PI, Vargemezis G, Papazachos CB, Tsokas GN. 2007b. Nondestructive DC resistivity surveying using flat-base electrodes. *Near Surface Geophysics* **5**(4): 243–272.

Apostol TM. 2004. The tunnel of Samos. *Engineering and Science* **1**: 30–40.

Burns A.1971. The Tunnel of Eupalinus and the tunnel problem of Hero of Alexandria. *Isis* **62**(2): 172–185.

Colla C, Maierhofer C. 2000. Investigation of historic masonry via radar reflection and tomography. In *Eighth International Conference on Ground Penetrating Radar*, Gold Coast, Australia; 893–898.

Cosentino P, Martorana R. 2001. The resistivity grid applied to wall structures: first results. In *Proceedings of the 7th Meeting of the Environmental and Engineering Geophysical Society, European Section*, Birmingham, UK; 36–37.

Doerpfeld W. 1894. Die Ausgrabungen an der Enneakrunos. *Athenische Mitteilungen* **19**: 144–146.

Evans HB. 1999. Review of Hermann Kienast, *Die Wasserleitung des Eupalinos auf Samos*. *American Journal of Archaeology* **103**(1): 149–150.

Fabricius E. 1884. Altetumer auf der insel Samos. *Mitteilungen des Deutschen Archaologischen Institutes in Athens* **9**: 165–192.

Fraser DC. 1969. Contouring of VLF-EM data. *Geophysics* **34**(6): 958–967.

Frumkin A, Shimron A. 2006. Tunnel engineering in the Iron Age: geoarchaeology of the Siloam Tunnel, Jerusalem. *Journal of Archaeological Science* **33**(2): 227–237.

Goodfield J, Toulmin S. 1965. How was the Tunnel of Eupalinus aligned? *Isis* **56**(1): 46–55.

Guerin V. 1856. Description de l'ile de Patmos et de l'ile de Samos. August Durand, Libraire: Paris.

Karastathis VK, Karmis PN, Drakatos G, Stavrakakis G. 2002. Geophysical methods contributing to the testing of concrete dams. Application of the Marathon Dam. *Journal of Applied Geophysics* **50**: 247–260.

Kienast HJ. 1995. Die wasserleitung des Efpalinos auf Samos (Samos XIX). Deutsches Archaologisches Institut: Bonn.

Kienast HJ. 2005. The Aqueduct of Eupalinos on Samos. Greek Ministry of Culture Archaeological Receipts Fund: Athens.

Kim JH. 2009. DC2DPro-2D interpretation system of DC Resistivity Tomography. User's Manual and Theory. Korean Institute of Geoscience and Mineral Resources: Daejeon.

Mol L, Preston P. 2010. The writing's in the wall: a review of new preliminary applications of electrical resistivity tomography within archaeology. *Archaeometry* **52**(6): 1079–1095.

Parker D. 1986. Lateral Resolution Structure and Seismic Velocity. Elsevier Science: Amsterdam.

Psilovikos A, Seitanidis G, Psilovikos A, Vavliakis E, Margoni S. 2003. The Eypalinion tunnel in Samos: a water-supply construction with karst dynamics behaviour. In *3rd Panhellenic Cave Symposium*, November 2003, Athens.

Sasaki Y, Matsuo K. 1993. Surface-to-tunnel resistivity tomography at the Kamaishi Mine. *Batsuri-Tansa* **46**(2): 128–133.

Sass O. 2005. Rock moisture measurements: techniques, results, and implications for weathering. *Earth Surface Processes and Landforms* **30**: 359–374.

Sass O, Viles HA. 2006. How wet are these walls? Testing a novel technique for measuring moisture in ruined walls. *Journal of Cultural Heritage* **7**: 257–263.

Soupios PM, Papazachos CB, Juhlin C, Tsokas GN. 2001. Nonlinear three-dimensional traveltime inversion of crosshole data with an application in the area of Middle Urals. *Geophysics* **66**: 627–636.

Stiros SC. 2006. Accurate measurements with primitive instruments: the 'paradox' in the qanat design. *Journal of Archaeological Science* **33**: 1058–1064.

Stiros SC. 2009. Orientation and alignment of the 5th century BC tunnel of Eupalinus at Samos (Greece). *Survey Review* **41**: 218–225.

Stiros SC. 2011. Levelling in antiquity: instrumentation, techniques and accuracies. *Survey Reviews* **44**: 45–52.

Tsokas GN, Tsourlos PI. 2007. Non-destructive electrical resistivity tomography survey at the south wall of Acropolis Athens. *Studijne zvesti archeologickeho ustvu sav* **41**: 250–252.

Tsokas GN, Tsourlos PI, Papadopoulos N, Manidaki V, Ioannidou M, Sarris A. 2006. Non-destructive ERT survey at the south wall of the Akropolis of Athens. *Extended Abstracts of Near Surface 2006*, Helsinki; B040.

Tsourlos PI. 1995. Modelling, interpretation and inversion of multielectrode resistivity survey data. Ph. D. Thesis, University of York, U.K.

Tsourlos PI, Tsokas GN. 2007. Archaeological prospection by means of fully non-destructive DC resistivity surveying. *Studijne zvesti archeologickeho ustvu sav* **41**: 252–254.

Tsourlos PI, Tsokas GN. 2011. Non-destructive electrical resistivity tomography survey at the south walls of the Acropolis of Athens. *Archaeological Prospection* **18**: 173–186.

Van der Waerden BL. 1968. Eupalinos and his tunnel. *Isis* **59**(1): 82–83.

Van Schoor M, Binley A. 2010. In-mine (tunnel-to-tunnel) electrical resistance tomography in South African platinum mines. *Near Surface Geophysics* **8:** 563–574.

Viles H, Sass O, Mol L. 2008. 2D resistivity surveys as a tool for investigating moisture in historic masonry walls. *SMW08 International workshop 'In situ Monitoring of Monumental Surfaces'*, Florence, Italy, 27–29 October; 91–96.

Yi M-J, Kim J-H, Chung K-L. 2003. Enhancing the resolving power of least-squares inversion with active constraint balancing. *Geophysics* **68**(3): 931–941.

Wait JR. 1982. Geo-electromagnetism. Academic Press Inc: London.

Zambas K. 2009. Final study for the restoration, final architectonical study for shaping and implementation study of the Eupalinina tunnel in Samos. KE N5400-4180-B-R-D-1-A-EE1, Greek Ministry of Culture: Athens. (In Greek.)

DOI: 10.1002/arp